Amorphous Cobalt Boride (Co_2B) as a Highly Efficient Nonprecious Catalyst for Electrochemical Water Splitting: Oxygen and Hydrogen Evolution

Justus Masa, Philipp Weide, Daniel Peeters, Ilya Sinev, Wei Xia, Zhenyu Sun, Christoph Somsen, Martin Muhler, and Wolfgang Schuhmann**

It is demonstrated that amorphous cobalt boride (Co_2B) prepared by the chemical reduction of $CoCl_2$ using $NaBH_4$ is an exceptionally efficient electrocatalyst for the oxygen evolution reaction (OER) in alkaline electrolytes and is simultaneously active for catalyzing the hydrogen evolution reaction (HER). The catalyst achieves a current density of 10 mA cm^{-2} at 1.61 V on an inert support and at 1.59 V when impregnated with nitrogen-doped graphene. Stable performance is maintained at 10 mA cm^{-2} for at least 60 h. The optimized catalyst, Co_2B annealed at 500 °C (Co_2B-500) evolves oxygen more efficiently than RuO_2 and IrO_2, and its performance matches the best cobalt-based catalysts reported to date. Co_2B is irreversibly oxidized at OER conditions to form a CoOOH surface layer. The active form of the catalyst is therefore represented as CoOOH/Co_2B. EXAFS observations indicate that boron induces lattice strain in the crystal structure of the metal, which potentially diminishes the thermodynamic and kinetic barrier of the hydroxylation reaction, formation of the OOH* intermediate, a key limiting step in the OER.

1. Introduction

The most advanced green means to generate H_2 from water is electrolysis, which requires the use of catalysts at both the anode and cathode of the water electrolyzer. However, to date, no catalysts exist that combine cost effectiveness, high performance, and long-term durability, which impedes the competitiveness of large-scale hydrogen and oxygen production through electrochemical water splitting.[1,2] The state-of-the art catalysts for the oxygen evolution reaction (OER), the anode reaction during water electrolysis, are typically RuO_2 and IrO_2,[3–6] while platinum-based alloys are used at the cathode for the hydrogen evolution reaction (HER).[5,7] Owing to the scarcity and high cost of precious metals, vigorous efforts have been pursued to develop low-cost and readily available electrocatalysts for water splitting.[4,8] Consequently, several classes of nonprecious electrocatalysts for OER have been developed, including some d-block transition metal oxides and hydroxides,[9] as well as non-metal-based OER catalysts.[10] Although RuO_2 and IrO_2 still command superior performance for OER in acidic electrolytes, recent studies have reported tremendous improvement of OER catalyzed by nonprecious catalysts in alkaline electrolytes with activity and stability benchmarks surpassing RuO_2 and IrO_2 by incorporating a non-metal element (e.g., N, S, P, Se) in the oxide, or hydroxide structure of cobalt[11–15] or nickel.[2,16–19] Intriguingly, these materials also exhibit exceptionally good activity towards hydrogen evolution,[20] which essentially unveils "a new chemistry" of materials for water splitting. Here, we demonstrate that amorphous cobalt boride (Co_2B) synthesized by the chemical reduction of $CoCl_2$ using $NaBH_4$, in accordance with the reaction, $2CoCl_2 + 4NaBH_4 + 9H_2O \rightarrow Co_2B + 4NaCl + 12.5H_2 + 3B(OH)_3$,[21,22] is exceptionally active in catalyzing the OER. When annealed at 500 °C (Co_2B-500), this catalyst evolves oxygen more efficiently than RuO_2 and IrO_2, achieving a current density of 10 mA cm^{-2} at 1.61 V_{RHE} on an inert support (glassy carbon) and 1.59 V_{RHE} when impregnated with nitrogen-doped graphene (Co_2B-500/NG). In addition, the catalyst maintained stable performance during electrolysis at 10 mA cm^{-2} for at least 60 h. This performance, to the best of our knowledge, is

Dr. J. Masa, Dr. Z. Sun, Prof. W. Schuhmann
Analytical Chemistry – Center for Electrochemical Sciences (CES)
Faculty of Chemistry and Biochemistry
Ruhr-Universität Bochum
D-44780 Bochum, Germany
E-mail: justus.masa@rub.de; wolfgang.schuhmann@rub.de

P. Weide, Dr. I. Sinev, Dr. W. Xia, Prof. M. Muhler
Laboratory of Industrial Chemistry
Faculty of Chemistry and Biochemistry
Ruhr-Universität Bochum
D-44780 Bochum, Germany

D. Peeters
Chair of Inorganic Chemistry II
Faculty of Chemistry and Biochemistry
Ruhr-Universität Bochum
D-44780 Bochum, Germany

Dr. C. Somsen
Chair of Materials Science and Engineering
Institute for Materials
Faculty of Mechanical Engineering
Ruhr-Universität Bochum
D-44780 Bochum, Germany

DOI: 10.1002/aenm.201502313

among the best reported for a cobalt-based catalyst and matches the benchmarks reported for P and Se containing cobalt catalysts.[14,23] Furthermore, the catalyst exhibits good activity for H_2 evolution and its practicability for deployment as an electrocatalyst at both the anode and cathode of a water splitting device was demonstrated in a single compartment two-electrode electrolyzer. A cell voltage of 1.81 V was achieved during electrolysis at a current density of 10 mA cm^{-2} in 3 M KOH and no loss in performance was observed after 53 h of continuous testing at different current densities.

2. Results and Discussion

To prepare Co_2B, a deaerated solution of 1 M $NaBH_4$ in 0.1 M NaOH was slowly added to deaerated 0.5 M $CoCl_{2(aq)}$. A dark precipitate formed immediately and was collected by filtration, washed several times with ultrapure water and ethanol, and stored in acetone until use. The vacuum dried product was pyrophoric (see Supporting Information for details).

ICP-AES analysis (Table 1S, Supporting Information) revealed that the product comprised of B (7.17 wt%) and Co (74.3 wt%), the rest being mostly oxygen, which corresponds to a Co:B atomic ratio of 1.9:1, thus indicating the formation of Co_2B.[22]

The composition of Co and B increased to 82.41 and 7.20 (wt%), respectively, when Co_2B was annealed at 500 °C for 2 h under argon (Co_2B-500). This increase is attributed to the loss of water from the synthesis. The BET surface area of Co_2B was 11.87 $m^2 g^{-1}$, which decreased to 9.26 $m^2 g^{-1}$ and 1.21 $m^2 g^{-1}$ upon annealing at 500 °C and 1000 °C, respectively. The SEM images in Figure S1 (Supporting Information) show the morphological properties of Co_2B, Co_2B-500, and Co_2B annealed at 1000 °C (Co_2B-1000), and the corresponding EDX spectra of Co_2B and Co_2B-500. EDX analysis revealed the presence of Co, B, and O as expected, and some carbon. The presence of carbon is attributed to contact of the product with ethanol and acetone, during washing and storage, respectively. The SEM images reveal pronounced changes in the particle morphology upon annealing, from very fine ultrathin particles of nonannealed Co_2B, to large aggregates of Co_2B annealed at 500 °C, and to a fully-agglomerated network of tubular-like structures of Co_2B annealed at 1000 °C.

XRD studies (**Figure 1**a) show that Co_2B is formed as an amorphous product, and remains XRD amorphous when annealed at <400 °C under He in agreement with the

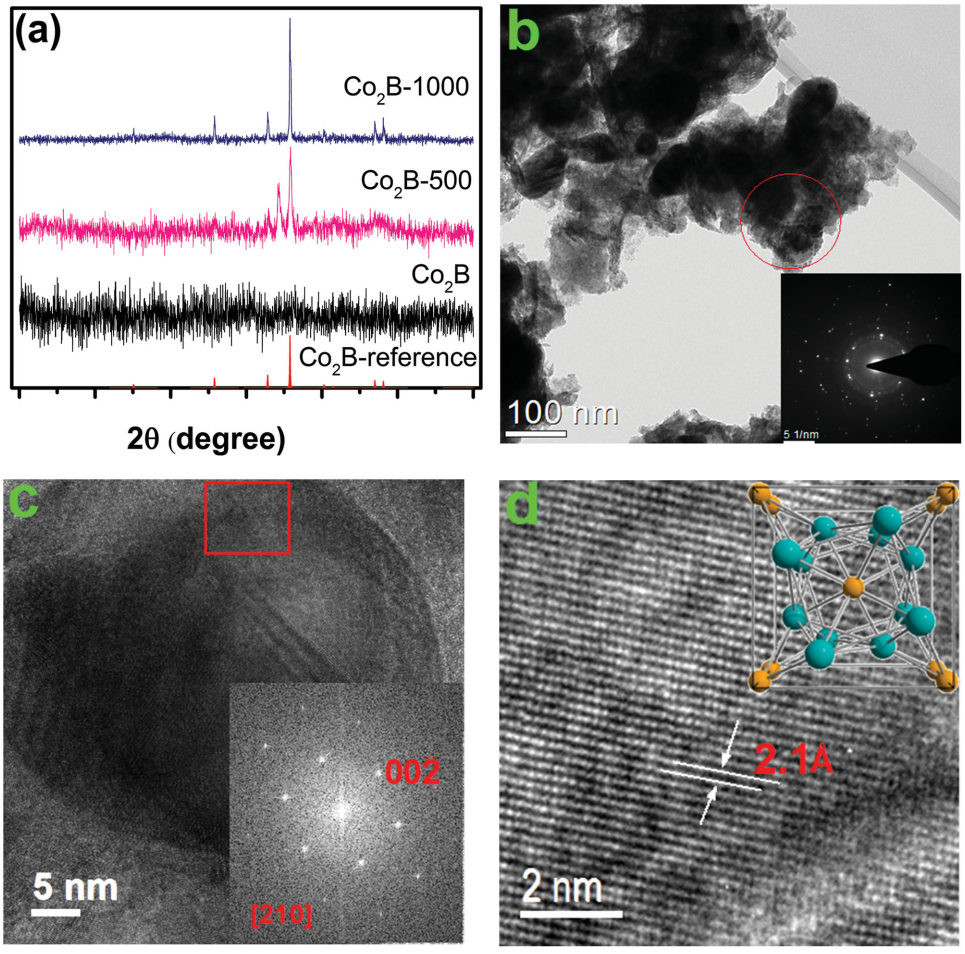

Figure 1. Effect of annealing temperature on the crystal structure of a) Co_2B, b) bright-field TEM image of Co_2B-500 with the SAED pattern of the circular marked region shown in the inset, c) HRTEM image of Co_2B-500 with the inset showing the SAED pattern of the square marked region along the [210] zone axis, d) HRTEM image of Co_2B-500 with the inset showing the unit cell structure of Co_2B.

literature.[24] When annealed at 500 °C, diffraction patterns indexed to Co_2B (ICSD 42531) emerge, while at 1000 °C, highly crystalline Co_2B (ICSD 42531) was formed, thus conclusively confirming that Co_2B was the main product of the synthesis.

TEM analysis of Co_2B-500 (Figure 1b) revealed discrete particles in an extensive amorphous layer in good agreement with XRD analysis. The selected area electron diffraction (SAED) pattern of the marked circular region (Inset Figure 1b) disclosed the existence of nanocrystalline phases. Fast Fourier-transformed (FFT) patterns of selected areas of an individual particle (Figure 1c) and the lattice spacing (2.1 Å) of the crystals along the [210] zone axis reveal a tetragonal structure, space group I –4 2 m, consistent with the structure of Co_2B.

Interrogation of the chemical surface state of Co_2B using XPS shows the main binding energies of the Co $2p_{3/2}$ and Co $2p_{1/2}$ core peaks at 778.07 and 793.19 eV, respectively (**Figure 2**a), essentially indistinguishable from the corresponding peaks for elemental cobalt (Co^0) as is expected in cobalt borides.[25,26] The Co $2p_{3/2}$ and Co 2p1/2 peaks at 780.83 and 796.75 eV respectively, are due to Co^{2+}, which indicates the presence of CoO or $Co(OH)_2$ inadvertently formed due to the preparation procedure and atmospheric exposure.[27] The main Co $2p_{3/2}$ of Co_2B-500 at 778.52 eV manifests a positive chemical shift of 0.45 eV relative to that of Co_2B thus indicating modulation of the electronic surface properties by the thermal annealing process. The Co $2p_{3/2}$ peak of Co_2B-500 at 778.52 eV agrees very well with that observed by Mavel et al. at 778.40 eV for crystalline Co_2B.[25] The ratio of Co:B in Co_2B calculated from the XPS data was 1.7, and 1.8 for Co_2B-500, which is in good agreement with the ICP-AES results. The B 1s spectrum of Co_2B was deconvoluted into two distinct species at 187.7 and at 191.5 eV (Figure 2b). The former is assigned to the interaction of boron with cobalt while the latter is due to boron-oxo species.[25,28] The prevalence of surface oxides is consistent with the core–shell structure proposed for amorphous metal borides, where a thin hydroxide or oxide film envelops metal boride particles.[29]

X-ray absorption measurements on Co_2B and Co_2B-500 give further insight into the chemical structure of the catalysts. The pre-edge region formed due to 1s to 3d electron transition (**Figure 3**a) has one peak (A) whose position exactly matches that of the Co-foil reference. However, the intensity of the pre-edge feature as well as the edge position and the slope indicate that the average oxidation state of Co is higher than 0. Moreover, both samples show a significant peak above the absorption edge indicating a considerable amount of oxidized cobalt to be present. Co–Co backscattering events dominate the extended X-ray fine structure (EXAFS) of Co_2B-500 (Figure 3b). There are also indications of light backscattered from cobalt in the first coordination sphere. The low distance peak at $r = 1.4$ Å is presumably due to both Co–O and Co–B backscattering events. Although the presence of boron in the first coordination sphere is not clearly evident, it can be distinguished by the broader and lower intensity peak indicating the interference of two waves with almost equal period, but shifted in phase to

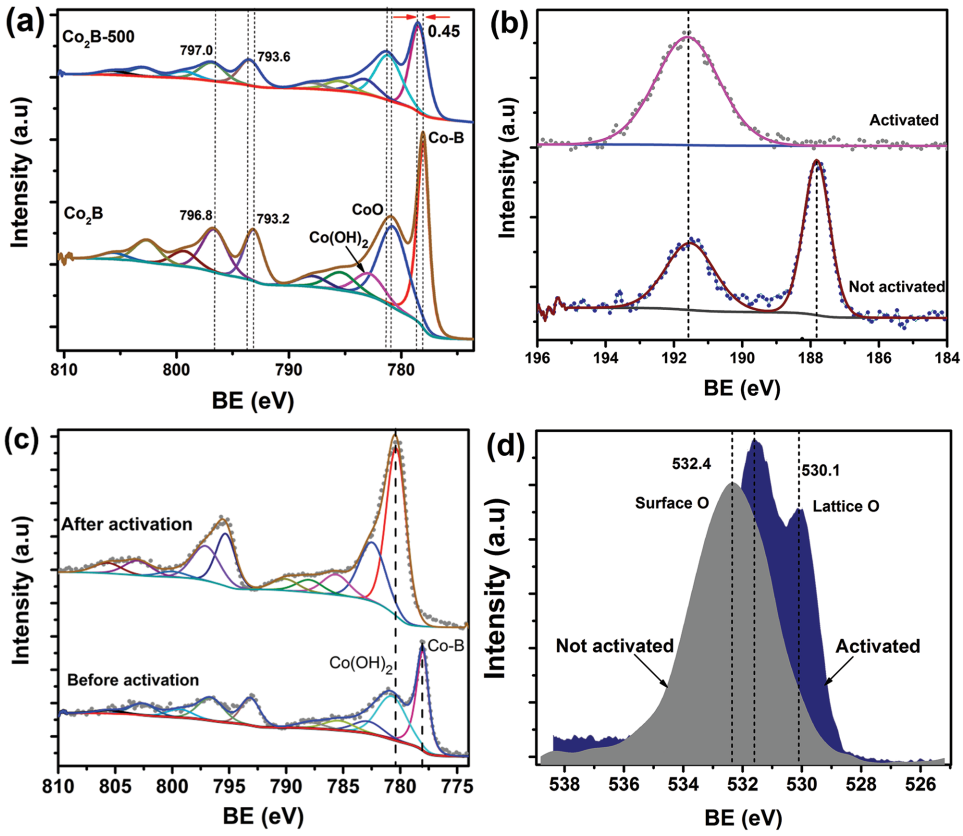

Figure 2. XPS analysis: Co 2p core-level spectra of Co_2B and of Co_2B annealed at 500 °C under He for 2 h (Co_2 B-500) a), b,c) B 1s and Co 2p core-level spectra of Co_2B-500, respectively, before and after activation, and d) O 1s high-resolution spectra of Co_2B-500 before and after electrochemical activation.

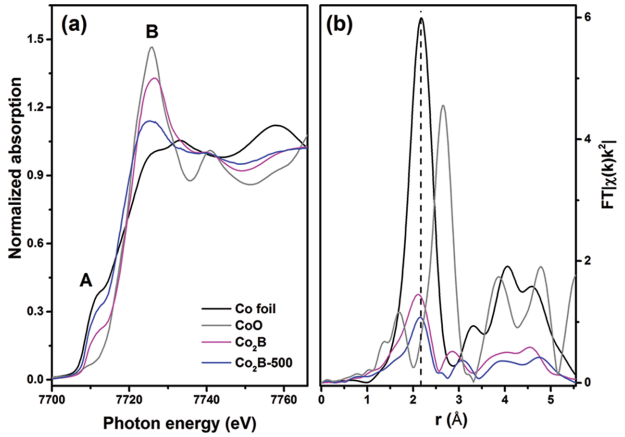

Figure 3. a) XANES and b) EXAFS spectra of Co_2B, Co_2B-500 and references Co foil (black) and CoO (gray).

form a not perfectly favorable interference pattern. The EXAFS spectra can be fitted using a Co–Co scattering pair to describe the main signal at 2.1 Å. The fit parameters are summarized in **Table 1**. The coordination numbers obtained are significantly lower than the reference for metallic Co indicating small particle sizes. Importantly, the bond distances obtained are longer than those for the reference compounds indicating crystal lattice strain. The lower r signals can however be described using both CoO and Co_2B structure models without any substantial change in the goodness of fit. It is expected that the strain exerted on the crystal lattice of cobalt by boron directly arises from their chemical interaction involving electron transfer and hybridization of B 2p states with the metal d orbitals. Moreover, intraelectron transfer between boron and cobalt due to interstitial boron atoms is also believed to be possible.[30]

The electrochemical behavior of the materials was investigated in KOH (0.1 M) with a loading of 0.21 mg cm^{-2} on

Table 1. CoK-edge EXAFS fitting of Co_2B and Co_2B-500.

Sample	Shell	Parameter	Co + Co_2B 6*Co 2.49 4*B 2.15	Co + CoO 6*Co 2.49 4*B 2.13
Co_2B	Co–Co	*R* [Å]	2.48	2.48
		CN	2.90	3.07
		δ^2	0.0069	0.0072
		ΔE [eV]	−4.84	−5.12
	Co–B	*R* [Å]	2.10	2.00
		CN	2.13	2.35
		δ^2	0.016	0.010
		ΔE [eV]	−11.13	−7.18
Co_2B-500	Co–Co	*R* [Å]	2.46	2.45
		CN	2.15	1.93
		δ^2	0.0062	0.0052
		ΔE [eV]	−3.21	−8.04
	Co–B	*R* [Å]	2.27	2.26
		CN	3.29	5.28
		δ^2	0.008	0.008
		ΔE [eV]	3.64	13.03

R is the distance from the central Co atom to the backscattering atom, CN is the apparent coordination number, $\sigma 2$ is the Debye–Waller factor, ΔE is adjustable "muffin-tin zero."

glassy carbon (for details see Supporting Information). Before collecting any activity data, the electrodes were continuously cycled between 0.8 V and 2.0 V vs RHE at 100 mV s^{-1} until reproducible voltammograms were obtained (Figure 5S, Supporting Information). During the first cycle of the conditioning process, a pronounced oxidation wave is observed between 1.1 and 1.6 V, which is drastically reduced in intensity in the subsequent cycles indicating that the catalyst becomes irreversibly oxidized to a higher oxidation state.[31] The peaks associated with the reversible redox process $Co(OH)_2 + OH^- \leftrightarrow CoOOH + H_2O + e$, occur between 1.0 and 1.3 V and progressively increase in intensity with cycling ultimately reaching a steady state (**Figure 4**a). This increase in intensity relates to continuous growth of a hydroxide/oxyhydroxide layer on Co_2B. XPS studies on the activated samples reveal predominance of oxidized states of B (Figure 2b) and Co (Figure 2c). In particular, the O 1s peak (Figure 2d) shows a clear transition from a surface dominated by adsorbed oxygen species with the main O 1s peak at 532.4 eV to a one dominated by lattice oxygen species, a CoOOH–like surface structure,[32,33] with two prominent peaks at 531.6 and 530.1 eV. Post analysis of the catalyst by ICP-AES after activation by cyclic voltammetry and after long-term stability studies revealed that the Co:B atomic ratio was unchanged (Table 1S, Supporting Information). Therefore, growth of the surface oxide/hydroxide layer did not alter the initial stoichiometry of the catalyst, an indication that the oxide species essentially dominate on the surface of the catalyst and that boron remains an inherent part of the active catalyst. The active form of the catalyst during the OER is therefore represented as $CoOOH/Co_2B$.

Evolution of an oxide/hydroxide (shell) surrounding a Ni_2P core under OER conditions was previously elucidated by Stern et al. by employing a combination of XPS depth profiling and HRTEM/EDX pre-and post-mortem elemental analysis, where the oxide/hydroxide shell was attributed to be responsible for OER.[16] Relatedly, Chang et al. observed a CoO_x surface oxide layer on the surface of cobalt phosphide (CoP) particles employed as bifunctional HER and OER catalysts for water splitting, and the oxide layer was believed to be responsible for catalysis of the OER.[33]

Figure 4b shows iR_s corrected linear sweep voltammograms (LSVs) of oxygen evolution by Co_2B, and Co_2B annealed at 500 and 1000 °C in He for 2 h (for LSVs at other annealing temperatures and details of iR_s correction, see Supporting Information). The LSVs were recorded in oxygen saturated 0.1 M KOH at a scan rate of 10 mV s^{-1} and 1600 rpm electrode rotation to avoid accumulation of gas bubbles on the electrode. Co_2B exhibited very high activity towards OER, which increased with annealing temperature, reaching a maximum at 500 °C, and decreasing sharply at higher temperatures. Figure 4c shows the evolution of the OER activity of Co_2B with annealing temperature. Co_2B-500 attained a current density of 10 mA cm^{-2} at as low as 1.61 V, which is exceptionally good for a cobalt-based catalyst on an inert support and without any conductive additive. Wu et al. reported similarly high activity, 1.62 V at 10 mA cm^{-2}, for cobalt nanoparticles prepared by post-reductive annealing at 600 °C. However, in this study the cobalt nanoparticles were supported on high surface area carbon.[34] By impregnating Co_2B-500 with 30 wt% nitrogen doped graphene (Co_2B-NG) as a conductive matrix, a 20 mV decrease in the overpotential down to 1.59 V at 10 mA cm^{-2} was achieved (Figure 4d). The

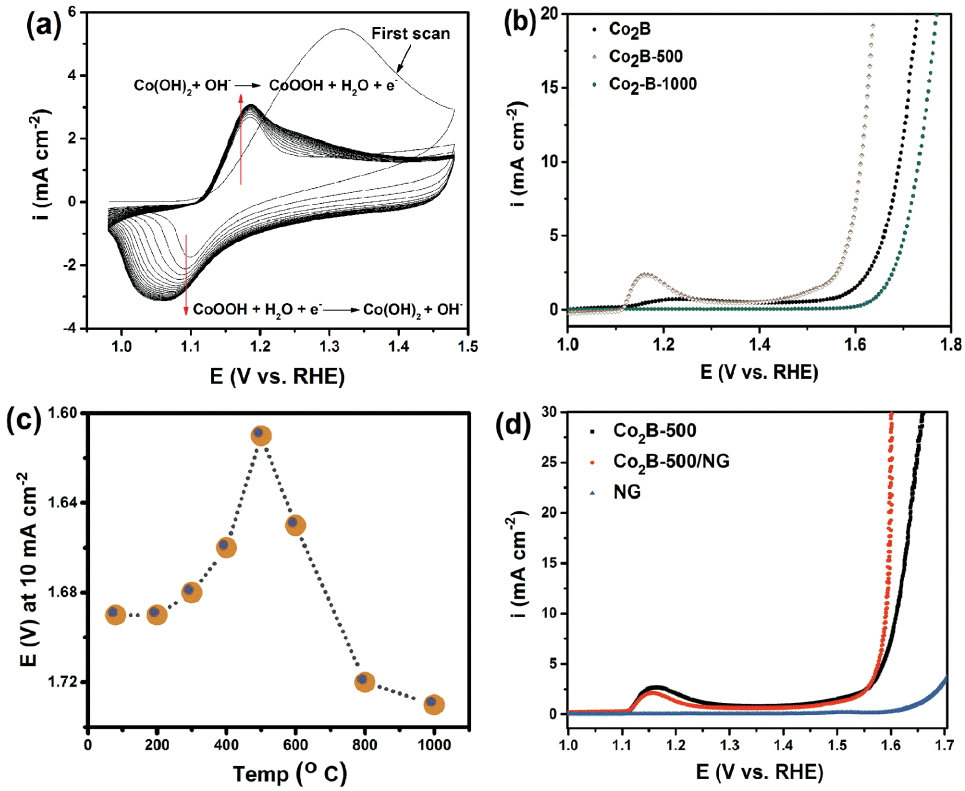

Figure 4. a) Activation of Co_2B by continuous potential cycling of between 1.0 V and 1.5 V at 100 mV s^{-1} in oxygen saturated 0.1 M KOH, b) Linear sweep voltammograms (corrected for the resistance of the electrolyte, iR_s) of Co_2B, and Co_2B annealed at 500 °C and 1000 °C recorded at 10 mV s^{-1} in O_2-saturated KOH (0.1 M) and at 1600 rpm electrode rotation as representative examples of the effect of annealing temperature on the OER activity of Co_2B, c) the OER activity of Co_2B as a function of the annealing temperature under He for 2 h, and d) comparative iRs corrected voltammograms of Co_2B-500, nitrogen-doped graphene (NG) and Co_2B-500 mixed with NG (Co_2B-500/NG) in a 3:7 weight ratio (NG: Co_2B-500).

nitrogen-doped graphene displayed negligible OER activity in the investigated potential window. The enhanced activity of Co_2B–NG is therefore attributed to improved charge transfer conferred by NG due to its high electrical conductivity. The BET surface area of Co_2B generally decreased with annealing temperature. For example, the BET area decreased from 11.87 m^2 g^{-1} for nonannealed Co_2B, to 9.70 m^2 g^{-1} and 1.2 m^2 g^{-1} for the catalyst annealed at 500 °C and 1000 °C, respectively. However, the OER activity of Co_2B-500 was much higher than that of Co_2B despite its clearly smaller BET area. Therefore, the increment in OER activity with annealing temperature up to 500 °C cannot be explained in terms of surface area. Amorphous materials are generally less electrically conductive compared to their crystalline counterparts. We expect that the sintering process instigated by annealing did not only lead to particle agglomeration as evidenced by the SEM images in Figure S1 (Supporting Information) but also caused improvement of electrical conductivity. Therefore, enhancement of charge transfer due to improved conductivity should have contributed to the observed enhanced in OER activity with annealing temperature. For example, as one can see in Figure 4b, the oxidation wave associated with the transition from $Co^{(II)}$ to $Co^{(III)}$, which occurs between 1.1 and 1.2 V is markedly more pronounced in the case of Co_2B-500 compared to the other catalysts, which is majorly attributed to its better conductivity. As observed by XRD, transition from XRD amorphous Co_2B to crystalline Co_2B commences at about 500 °C, which is expected to be accompanied with enhancement of electrical conductivity. Additionally, the positive chemical shift of 0.45 eV in the binding energy of the Co 2p3/2 core level upon annealing at 500 °C manifests a transformation of the electronic surface structure of Co_2B by the annealing process. This is also expected to have contributed to the observed enhancement in OER activity. On the other hand, the decline in OER activity at higher annealing temperatures is mainly due to growth in particle size and decrease in the surface area. For example, the BET area of Co_2B-1000 was only 1.2 m^2 g^{-1} and the particles sizes were distinctly much larger (Figure S1, Supporting Information).

To give some perspective of Co_2B-500, its performance was compared against Co_3O_4, electrodeposited $Co(OH)_2$ and RuO_2 measured under similar conditions (**Figure 5**a). Co_3O_4, $Co(OH)_2$, and RuO_2 attained 10 mA cm^{-2} at 1.71 V, 1.74 V, and 1.62 V, respectively. Co_2B-500 is thus markedly more active than Co_3O_4 and $Co(OH)_2$.[35] More interestingly, Co_2B also attains 10 mA cm^{-2} at a lower overpotential (0.38 V) than RuO_2 (0.40 V), which is remarkable for a nonprecious metal-based catalyst. Figure 5b summarizes the activity of Co_2B-500 and Co_2B/NG expressed as the overpotential (η) at 10 mA cm^{-2}, against IrO_2 and RuO_2 in the form of bar graphs. The Tafel slope of Co_2B-500 (45.0 mV dec^{-1}), computed from slow scan voltammograms (1 mV s^{-1}), significantly contrasts that of Co_3O_4 (82.6 mV dec^{-1}) and $Co(OH)_2$ (64.8 mV dec^{-1})

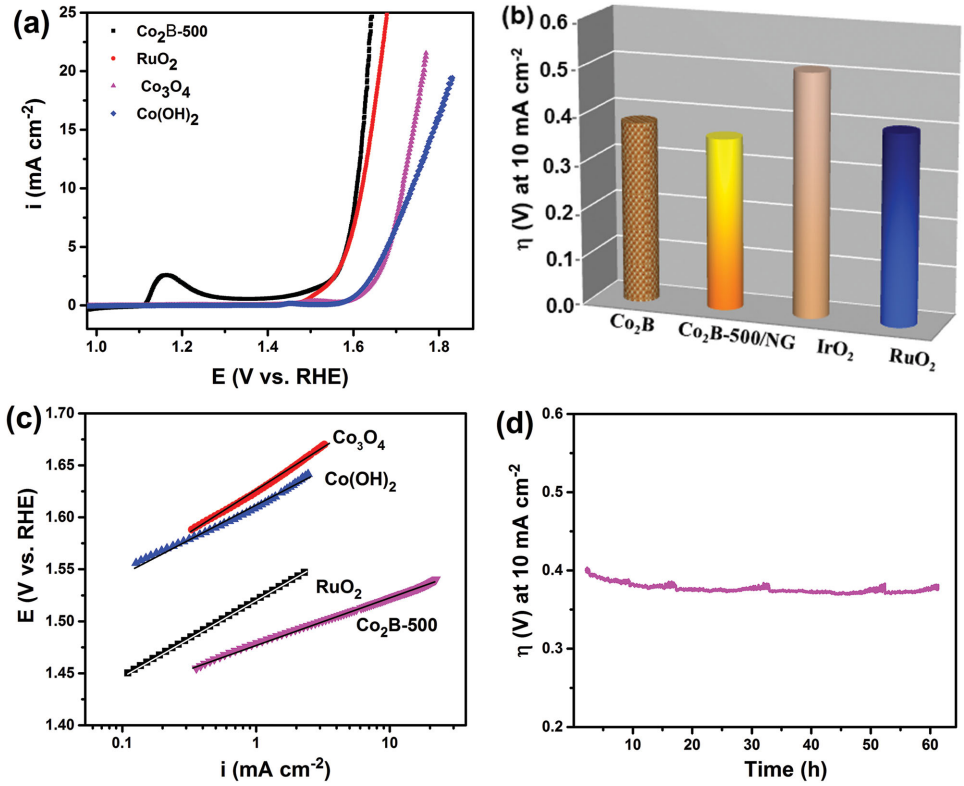

Figure 5. a) Comparison of the OER activity of Co_2B-500 against Co_3O_4, electrodeposited $Co(OH)_2$ and RuO_2, b) a bar graph of the overpotential (η) at 10 mA cm^{-2} of Co_2B-500, Co_2B-500/NG, RuO_2 and IrO_2, c) Tafel plots of Co_2B-500, RuO_2, IrO_2, Co_3O_4 and $Co(OH)_2$, and d) galvanostatic stability test (iR_s corrected potential) of Co_2B-500 at a current density of 10 mA cm^{-2} in oxygen saturated 0.1 M KOH under continuous electrode rotation at 1600 rpm. The potential was corrected for iR_s drop.

and was also lower than that of RuO_2 (62.3 mV dec^{-1}) further underscoring the superiority of this catalyst (Figure 5c). More detailed comparison of the performance of the present catalyst with recently published literature is summarized in Table S2 (Supporting Information). Notably, the performance of Co_2B-500 compares favorably with that of the most active cobalt-based catalysts, including NG-$CoSe_2$[13] and CoP/NF[12] where overpotentials of 0.37 V and 0.39 V, respectively, were reported at a current density of 10 mA cm^{-2}. Lower potentials of 0.29 V and 0.32 V have been reported for $CeO_2/CoSe_2$[15] and $CoSe_2$[11] as well as CoP-NR,[33] respectively. Unprecedentedly low overpotentials have recently been reported for cobalt- and nickel-based catalysts supported on nickel foam.[12,16,18] However, nickel foam is intrinsically an active OER catalyst and is thus expected to substantially contribute to the measured activity. It is therefore difficult to deduce the intrinsic activity of catalysts supported on nickel foam in order to make a fair comparison with catalysts supported on inert supports. To investigate the influence of the support substrate on the OER, 21 µL of a catalyst ink prepared according to the procedure described in Section 2.4 (Supporting Information) was drop coated on a clean rectangular piece of FTO glass covering an area of 1.0 × 0.5 cm^2 resulting in a catalyst loading of 210 µg cm^{-2} similar to that used for glassy carbon electrodes. After drying in air for 30 min voltammograms were recorded in oxygen saturated 0.1 M KOH at a scan rate of 10 mV s^{-1}. The OER results of Co_2B-500 supported on FTO glass are presented in Figure S9 (Supporting Information). The potential required to reach a current density of 10 mA cm^{-2} was 1.68 V, which is significantly higher compared to the value of 1.61 V obtained with the catalyst supported on glassy carbon. This discrepancy most likely arises from impeded charge transfer on FTO due to its relatively lower electrical conductivity compared to glassy carbon. Therefore, only results on glassy carbon are presented and discussed hereafter.

It is worth to note the chemical similarity between the present catalyst (Co_2B) and $CoSe_2$,[15,23,36] CoP,[12,14] and $CoSe_2$,[11,15] as well as Ni_2P[16] and Ni_2S,[18] which were recently reported to possess very high OER activity surpassing their respective pure oxides and hydroxides and even RuO_2 and IrO_2. The distinctive performance of these compounds suggests that whereas physical factors such as conductivity, structural disorder (or defects), and surface area may strongly influence OER activity, the nonmetallic components, S, P, and Se, appear to bear an intrinsic role in enhancing the activity of cobalt, which warrants explanation. Trace amounts of Fe contamination in the electrolyte or in nickel-based catalysts were observed to bear a significant influence on OER activity.[37] In the present studies, $Co(OH)_2$ and Co_3O_4 investigated in the same electrolyte were a lot less active. The predominance of Fe contamination in the electrolyte in promoting the observed OER activity can therefore be excluded. High OER activity of a Ni_2P catalyst was attributed to a unique Ni_2P (core)/NiO_x (shell) structure formed during OER, where the core provides effective electron transport to the

less conductive NiO_x shell.[16] Several authors have attributed high OER activity of cobalt and nickel catalysts containing a non-metal element(s), including N, P, S, and Se among others, to yet unexplained synergistic effects.[16,19]

The electrochemical oxidation of water by metals essentially takes place on a surface oxide/hydroxide layer.[38] For a given metal, spontaneous formation of an adsorbed hydroxide layer on the metal surface takes place when the metal is immersed in an alkaline electrolyte. The mostly widely accepted mechanism for oxygen evolution on transition metal oxides was proposed by Bockris and Otagawa.[38] In this mechanism, under oxidizing conditions, the initial step involves adsorption of OH^- ions and their discharge to form an adsorbed hydroxide layer, reaction (1). In the subsequent step, the adsorbed OH reacts with OH^- to form an oxide layer (MO) with the release of H_2O and an electron, reaction (2). This reaction is followed by a hydroxylation reaction involving reaction of the oxide layer with OH^- to form OOH species, an oxide-hydroxide layer, reaction (3). The oxide-hydroxide species undergoes reaction with OH^- to form adsorbed O_2 and H_2O with the release of an electron, reaction (4). The last step involves desorption of O_2, reaction (5). Reaction (3) has been suggested by many authors to be the rate limiting step during OER. Trasatti observed a positive correlation between OER activity and the enthalpy of transition of a given metal from a lower to a higher valency state in the metal oxide, which was proposed as an important catalytic descriptor for oxygen evolution on metal oxide surfaces.[39]

$$M + OH^- \rightarrow MOH + e^- \quad (1)$$

$$MOH + OH^- \rightarrow MO + H_2O + e^- \quad (2)$$

$$MO + OH^- \rightarrow MOOH + e^- \quad (3)$$

$$MOOH + OH^- \rightarrow MO_2 + H_2O + e^- \quad (4)$$

$$MO_2 \rightarrow M + O_2 \quad (5)$$

On the other hand, DFT calculations indicate that the most difficult step in water oxidation is the formation of (OOH)-type species, which are key intermediates during OER.[6] Lattice strain effects have previously been observed to influence electrocatalytic O_2 reduction on core–shell platinum alloy catalysts.[40] The strain induced by boron on the crystal lattice of cobalt atoms as observed by EXAFS could thus potentially diminish the energy barrier for oxidation of cobalt, thus rendering more facile formation of the OOH* intermediate during OER. Conservation of the Co:B atomic ratio after electrochemical testing as revealed by ICP–AES (Table 1S, Supporting Information) indicates that boron remains an inherent part of the catalyst structure during OER. Generally, if any role is played by boron in promoting OER activity, it has to accrue from its chemical interaction with cobalt. Studies show that in addition to lattice boron, interstitial boron may also exist in a given metal boride.[21] In the case of amorphous metal borides, as in the case of Co_2B in the present study, the charge density is concentrated in the M_2B plane (M=Co) indicating preferential bonding of boron to one of the metal atoms. In all these cases, theoretical calculations reveal significant hybridization of B 2p states with the 3d orbitals of the metal accompanied by concentration of charge between M—B and between B—B, and weakening of the M—M bonds.[30] This theoretical justification of the weakening of Co—Co bonds further underscores the importance of lattice strain in diminishing the energy barrier for formation of the OOH intermediate during OER. Meanwhile, we expect that improvement in electrical conductivity should have majorly contributed to the initial enhancement of OER activity with annealing up to 500 °C. After 500 °C, the decline in activity was mainly due to growth of particle size accompanied with decrease in surface area. Additionally, from the XPS data (Figure 2a), the observed electronic structure modulation manifested by a positive chemical shift of 0.45 eV in the binding energy of the Co $2p_{3/2}$ core peak upon annealing Co_2B at 500 °C indicates a transformation in the surface electronic structure. The contribution of surface electronic effects in promoting electrocatalytic reactions is well known. Therefore, the contribution of temperature induced electronic effects in promoting the observed enhancement of OER with annealing temperature ought to be considered.

The long-term performance of Co_2B-500 was investigated by galvanostatic polarization at 10 mA cm^{-2} in air saturated 0.1 M KOH. The system showed improvement in performance with time during the initial 17 h, and then maintained a very stable overpotential thereafter, essentially exhibiting no degradation for at least 60 h (Figure 5d). The activity gain during the initial 17 h arises from growth of the cobalt oxide/hydroxide layer (CoOOH), which is the active electrocatalytic layer for oxygen evolution. The stability of the catalysts was further assessed by continuous potential cycling up to 5000 cycles between 1.0 and 1.8 V at a scan rate of 100 mV s^{-1} with electrode rotation at 1600 rpm to prevent accumulation of gas bubbles on the electrode surface. The linear sweep voltammograms recorded before and after the 5000 cycles of testing at a slow scan rate of 10 mV s^{-1} are shown in Figure S8 (Supporting Information). There was only minimal loss in activity corresponding to about 10 mV at a current density of 10 mA cm^{-2}. There is therefore very good agreement between the galvanostatic stability test and the potential cycling stability test thus reaffirming that Co_2B-500 is a potentially very stable catalyst. The strong covalent character of metal-metalloid bonds in metal borides, which is responsible for their chemical inertness, extreme hardness and use as refractory materials, is expected to play a role in stabilizing the CoOOH/Co_2B system under OER conditions.

As a perspective, a glassy carbon electrode modified with Co_2B-500 was tested for the HER in 1 M KOH, and good activity was observed (**Figure 6**), in good agreement with recent results.[41] Despite the promising HER activity, Co_2B-500 exhibited a rather high overpotential compared to Pt/C. For example, Co_2B-500 requires an additional overpotential of 328 mV compared to Pt/C to deliver a current of –10 mA cm^{-2}. Interestingly, a significant reduction in HER overpotential, from 328 to 127 mV relative to Pt/C was achieved when Co_2B-500 was impregnated on nitrogen-doped graphene (NG). NG itself displayed negligible HER activity. The observed improvement in HER activity of Co_2B-500/NG is thus mainly attributed to enhancement of charge transfer due to the high electronic conductivity of NG. Impregnation of Co_2B-500 with NG did not only alter the kinetics of HER but also its mechanism as manifested by the marked change in the Tafel slope (Figure 6b). Co_2B-500 exhibited two distinctive Tafel slopes, 136.2 mV dec^{-1}

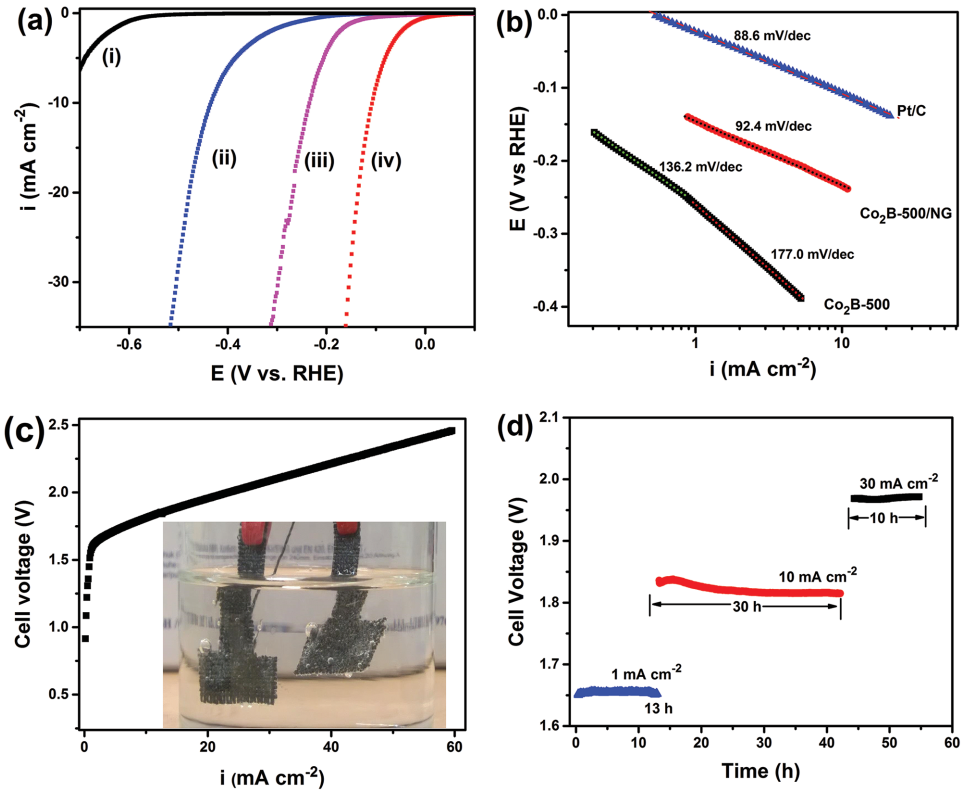

Figure 6. a) Linear sweep voltammograms showing hydrogen evolution catalyzed by glassy carbon modified with nitrogen-doped graphene (NG) (i), Co_2 B-500 (ii), Co_2B-500 impregnated with NG (Co_2 B-500/NG) (iii) and platinum nanoparticles (20%) supported on carbon black (Pt/C) (iv). The voltammograms (corrected for iR_s) were recorded in argon saturated 1.0 M KOH at a scan rate of 5 mV s^{-1} with electrode rotation at 1600 rpm, b) Tafel graphs of Co_2B-500, Co_2B-500/NG, and Pt/C as a reference, extracted from (a) c) complete water electrolysis in a single compartment two-electrode cell using Co_2B-500 supported on carbon cloth both as the anode, and Co_2B-500/NG on carbon cloth as the cathode in 3 M KOH as the electrolyte. The inset of (c) shows a photographic image of the cell during electrolysis, and d) chronopotentiometric stability curves at different current densities during electrolysis of water in a two electrode cell using Co_2B-500 supported on carbon cloth both as the anode and Co_2B-500/NG supported on carbon cloth as the cathode, and 3 M KOH as the electrolyte.

at lower current densities, and 177.0 mV dec^{-1} at higher current densities. By contrast, Co_2B-500/NG exhibited only one Tafel line with a slope of 92.4 mV dec^{-1}. The Tafel slope of Co_2B-500/NG was similar to that of Pt/C (88.6 mV dec^{-1}), which indicates that the mechanism of hydrogen evolution on Co_2B-500/NG was similar to that on Pt, but different from that on Co_2B-500. Three classical theories are routinely used to explain the mechanisms underlying hydrogen evolution on metal surfaces. The first step, the Volmer reaction, is generally believed to involve water discharge in accordance with the reaction $M + H_2O + e^- \rightarrow MH_{ads} + OH^-$, where M is the active site of the metal. The Tafel slope of this step is defined by $b = \frac{2.3RT}{\alpha F}$, and under standard conditions has a value of about 118.2 mV dec^{-1}, where R is the universal gas constant, T is the temperature (298 K), F is Faraday's constant, and assuming a value of 0.5 for the charge transfer coefficient α. The Volmer reaction is followed either by an electrochemical desorption step, the Heyrovsky reaction, $MH_{ads} + H_2O + e^- \rightarrow M + H_2 + OH^-$, or by a chemical recombination step, the Tafel reaction, $H_{ads} + H_{ads} \rightarrow H_2$. The Tafel slope associated with the Heyrovsky reaction is defined by $b = \frac{2.3RT}{(1+\alpha)F}$ and has a value of about 39.4 mV dec^{-1} while that of the Tafel reaction is defined by $b = \frac{2.3RT}{2F}$ and has a value of about 29.6 mV dec^{-1}.[42] Therefore, the water discharge reaction appears to be the dominant rate limiting step during the HER on all the catalysts.

To demonstrate the practicability of using Co_2B-500 as the anode electrocatalyst, and Co_2B-500/NG as the cathode electrocatalyst to achieve complete water electrolysis, a suspension of the catalysts, 20 mg mL^{-1} in a mixture of water, ethanol, and Nafion (5%) in the volume ratio of 49:49:2, respectively, was deposited on rectangular pieces of carbon cloth (1.0 cm × 0.7 cm) and deployed in a two electrode, single compartment cell with 3 M KOH as the electrolyte. Figure 6c shows a typical galvanostatic polarization curve recorded during the electrolysis test. The inset shows a photographic image of the electrodes during electrolysis at 10 mA cm^{-2}. Vigorous gas evolution was observed at both electrodes, (see video in Supporting Information) which increased in intensity with the applied current. The cell voltage in the lower current regime was in good agreement with the standard measurements performed in three-electrode cells (see Figure S10, Supporting Information). For example, at 10 mA cm^{-2}, the cell voltage was 1.81 V while at 30 mA cm^{-2} it was 2.04 V. Very stable cell voltages were observed during

successive electrolysis at 1, 10, and 30 mA cm^{-2} using the same pair of electrodes. The slight gain in activity observed during electrolysis at 10 mA cm^{-2} is attributed to activation of the catalyst due to growth of the oxide/hydroxide layer as demonstrated in Figure 4. At much higher current densities, the cell voltages were much higher than those encountered under industrial conditions, typically between 1.7 and 1.8 V at 100 mA cm^{-2}.[43] This may however be overcome by using a more conductive current collector, running the reaction in a zero-gap cell, and employing high temperatures and pressures similar to industrial conditions.

3. Conclusion

Amorphous cobalt boride (Co_2B) is unveiled as a very promising catalyst for water splitting, with exceptionally good performance for OER. The optimized catalyst annealed at 500 °C under He (Co_2B-500) evolved O_2 more efficiently than IrO_2 and RuO_2, and exhibited no loss in performance after over 60 h of continuous electrolysis at 10 mA cm^{-2}. The lattice strain induced in the crystal structure of the metal due to the presence of boron potentially reduces the energetic and kinetic barrier of the hydroxylation reaction, formation of the OOH* intermediate, a key limiting step in the OER. Complete water electrolysis tests using Co_2B-500 as the anode and Co_2B-500 supported on nitrogen-doped graphene as the cathode (Co_2B-500/NG) were demonstrated in a two-electrode cell and revealed vigorous gas evolution at moderate cell voltages and very stable performance. This study is therefore of both fundamental and practical importance as it introduces a new class of promising materials for deployment at both the anode and cathode of a water splitting device.

Supporting Information

Supporting Information is available from the Wiley Online Library or from the author.

Acknowledgements

Financial support from the DFG (Deutsche Forschungsgemeinschaft) in the framework of the Cluster of Excellence RESOLV (EXC1069), the Helmholtz-Energie-Allianz "Stationäre elektrochemische Speicher und Wandler" (HA-E-0002) and the Ruhr-Universität Research Department IFSC are gratefully acknowledged. The formatting of Table 1 was changed on April 4, 2016. The values contained were unchanged.

Received: November 19, 2015
Published online: January 7, 2016

[1] a) T. V. Vineesh, M. P. Kumar, C. Takahashi, G. Kalita, S. Alwarappan, D. K. Pattanayak, T. N. Narayanan, *Adv. Energy Mater.* **2015**, *5*, 1500658; b) I. Katsounaros, S. Cherevko, A. R. Zeradjanin, K. J. J. Mayrhofer, *Angew. Chem. Int. Ed.* **2014**, *53*, 102; c) E. Fabbri, M. Nachtegaal, X. Cheng, T. J. Schmidt, *Adv. Energy Mater.* **2015**, *5*, 1402033.

[2] J. Ren, M. Antonietti, T.-P. Fellinger, *Adv. Energy Mater.* **2015**, *5*, 1401660.

[3] a) J. Lee, B. Jeong, J. D. Ocon, *Curr. Appl. Phys.* **2013**, *13*, 309; b) Y. Leng, G. Chen, A. J. Mendoza, T. B. Tighe, M. A. Hickner, C.-Y. Wang, *J. Am. Chem. Soc* **2012**, *134*, 90547; c) Y. Lee, J. Suntivich, K. J. May, E. E. Perry, Y. Shao-Horn, *J. Phys. Chem. Lett* **2012**, 399; d) S. Park, Y. Shao, J. Liu, Y. Wang, *Energy Environ. Sci.* **2012**, *5*, 93314; e) M. Bernicke, E. Ortel, T. Reier, A. Bergmann, J. Ferreira de Araujo, P. Strasser, R. Kraehnert, *ChemSusChem* **2015**, *8*, 19085.

[4] C. C. L. McCrory, S. Jung, J. C. Peters, T. F. Jaramillo, *J. Am. Chem. Soc.* **2013**, *135*, 1697787.

[5] C. C. L. McCrory, S. Jung, I. M. Ferrer, S. M. Chatman, J. C. Peters, T. F. Jaramillo, *J. Am. Chem. Soc.* **2015**, *137*, 43477.

[6] J. Rossmeisl, Z.-W. Qu, H. Zhu, G.-J. Kroes, J. K. Nørskov, *J. Electroanal. Chem.* **2007**, *607*, 83.

[7] a) J. Greeley, T. F. Jaramillo, J. Bonde, I. B. Chorkendorff, J. K. Nørskov, *Nat. Mater.* **2006**, *5*, 909; b) H. A. Gasteiger, N. M. Markovic, *Science* **2009**, *324*, 48; c) Y. Zheng, Y. Jiao, M. Jaroniec, S. Z. Qiao, *Angew. Chem. Int. Ed.* **2015**, *54*, 52.

[8] Y. Jiao, Y. Zheng, M. Jaroniec, S. Z. Qiao, *Chem. Soc. Rev.* **2015**, *44*, 20606.
a) K. L. Nardi, N. Yang, C. F. Dickens, A. L. Strickler, S. F. Bent, *Adv. Energy Mater.* **2015**, *5*, 1500412; b) Z. Peng, D. Jia, A. M. Al-Enizi, A. A. Elzatahry, G. Zheng, *Adv. Energy Mater.* **2015**, *5*, 1402031; c) A. Zhao, J. Masa, W. Xia, A. Maljusch, M.-G. Willinger, G. Clavel, K. Xie, R. Schlögl, W. Schuhmann, M. Muhler, *J. Am. Chem. Soc.* **2014**, *136*, 75514; d) J. Masa, W. Xia, I. Sinev, A. Zhao, Z. Sun, S. Grützke, P. Weide, M. Muhler, W. Schuhmann, *Angew. Chem. Int. Ed.* **2014**, *53*, 85082; e) R. Frydendal, E. A. Paoli, I. Chorkendorff, J. Rossmeisl, I. E. L. Stephens, *Adv. Energy Mater.* **2015**, *5*, 1500991; f) M. Gong, Y. Li, H. Wang, Y. Liang, J. Z. Wu, J. Zhou, J. Wang, T. Regier, F. Wei, H. Dai, *J. Am. Chem. Soc.* **2013**, *135*, 84525; g) S. Cobo, J. Heidkamp, P.-A. Jacques, J. Fize, V. Fourmond, L. Guetaz, B. Jousselme, V. Ivanova, H. Dau, S. Palacin, M. Fontecave, V. Artero, *Nat. Mater.* **2012**, *11*, 802; h) F. Cheng, J. Shen, B. Peng, Y. Pan, Z. Tao, J. Chen, *Nat. Chem.* **2010**, *3*, 79; i) J. Nai, H. Yin, T. You, L. Zheng, J. Zhang, P. Wang, Z. Jin, Y. Tian, J. Liu, Z. Tang, L. Guo, *Adv. Energy Mater.* **2015**, *5*, 1401880.

[9] a) T. Y. Ma, J. Ran, S. Dai, M. Jaroniec, S. Z. Qiao, *Angew. Chem. Int. Ed.* **2015**, *54*, 46460; b) J. Zhang, Z. Zhao, Z. Xia, L. Dai, *Nat. Nanotechnol.* **2015**, *10*, 444.

[10] Y. Liu, H. Cheng, M. Lyu, S. Fan, Q. Liu, W. Zhang, Y. Zhi, C. Wang, C. Xiao, S. Wei, B. Ye, Y. Xie, *J. Am. Chem. Soc* **2014**, *136*, 1567075.

[11] Y.-P. Zhu, Y.-P. Liu, T.-Z. Ren, Z.-Y. Yuan, *Adv. Funct. Mater.* **2015**, *25*, 7395.

[12] M.-R. Gao, X. Cao, Q. Gao, Y.-F. Xu, Y.-R. Zheng, J. Jiang, S.-H. Yu, *ACS Nano* **2014**, *8*, 39708.

[13] J. Ryu, N. Jung, J. H. Jang, H.-J. Kim, S. J. Yoo, *ACS Catal.* **2015**, *5*, 40664.

[14] Y.-R. Zheng, M.-R. Gao, Q. Gao, H.-H. Li, J. Xu, Z.-Y. Wu, S.-H. Yu, *Small* **2015**, *11*, 182.

[15] L.-A. Stern, L. Feng, F. Song, X. Hu, *Energy Environ. Sci.* **2015**, *8*, 23471.

[16] a) K. Xu, P. Chen, X. Li, Y. Tong, H. Ding, X. Wu, W. Chu, Z. Peng, C. Wu, Y. Xie, *J. Am. Chem. Soc.* **2015**, *137*, 41195; b) C. Tang, N. Cheng, Z. Pu, W. Xing, X. Sun, *Angew. Chem. Int. Ed.* **2015**, *54*, 93515.

[17] W. Zhou, X.-J. Wu, X. Cao, X. Huang, C. Tan, J. Tian, H. Liu, J. Wang, H. Zhang, *Energy Environ. Sci.* **2013**, *6*, 29214.

[18] M. Shalom, D. Ressnig, X. Yang, G. Clavel, T. P. Fellinger, M. Antonietti, *J. Mater. Chem. A* **2015**, *3*, 81717.

[19] a) E. J. Popczun, J. R. McKone, C. G. Read, A. J. Biacchi, A. M. Wiltrout, N. S. Lewis, R. E. Schaak, *J. Am. Chem. Soc.* **2013**, *135*, 92670; b) J. Tian, Q. Liu, A. M. Asiri, X. Sun, *J. Am. Chem. Soc.* **2014**, *136*, 75870.

[20] S. Carenco, D. Portehault, C. Boissière, N. Mézailles, C. Sanchez, *Chem. Rev.* **2013**, *113*, 79815.
[21] B. Ganem, J. O. Osby, *Chem. Rev.* **1986**, *86*, 763.
[22] M.-R. Gao, Y.-F. Xu, J. Jiang, Y.-R. Zheng, S.-H. Yu, *J. Am. Chem. Soc.* **2012**, *134*, 29303.
[23] C. Wu, F. Wu, Y. Bai, B. Yi, H. Zhang, *Mater. Lett.* **2005**, *59*, 17481.
[24] G. Mavel, J. Escard, P. Costa, J. Castaing, *Surf. Sci.* **1973**, *35*, 109.
[25] P. Krishnan, K.-L. Hsueh, S.-D. Yim, *Appl. Catal., B* **2007**, *77*, 206.
[26] B. J. Tan, K. J. Klabunde, P. M. A. Sherwood, *J. Am. Chem. Soc.* **1991**, *113*, 855.
[27] a) S. Lu, Di Cao, X. Xu, H. Wang, Y. Xiang, *RSC Adv.* **2014**, *4*, 2694045; b) Y. Wang, M. Trenary, *Chem. Mater.* **1993**, *5*, 199; c) Y. Okamoto, Y. Nitta, T. Imanaka, S. Teranishi, *J. Chem. Soc., Faraday Trans. 1* **1979**, *75*, 20279.
[28] a) U. B. Demirci, P. Miele, *Phys. Chem. Chem. Phys.* **2010**, *12*, 1465165; b) J. Geng, D. A. Jefferson, Johnson, F. G. Brian, *Chemistry* **2009**, *15*, 11343; c) G. M. Arzac, T. C. Rojas, A. Fernández, *Appl. Catal., B* **2012**, *128*, 39; d) G. M. Arzac, T. C. Rojas, A. Fernández, *ChemCatChem* **2011**, *3*, 13053.
[29] G. P. Shveikin, A. L. Ivanovskii, *Russ. Chem. Rev.* **1994**, *63*, 711.
[30] L. D. Burke, M. E. Lyons, O. J. Murphy, *J. Electroanal. Chem.* **1982**, *132*, 247.
[31] J. Yang, H. Liu, W. N. Martens, R. L. Frost, *J. Phys. Chem. C* **2010**, *114*, 111.
[32] J. Chang, Y. Xiao, M. Xiao, J. Ge, C. Liu, W. Xing, *ACS Catal.* **2015**, *5*, 68748.
[33] L. Wu, Q. Li, C. H. Wu, H. Zhu, A. Mendoza-Garcia, B. Shen, J. Guo, S. Sun, *J. Am. Chem. Soc.* **2015**, *137*, 70714.
[34] Y. Wang, T. Zhou, K. Jiang, P. Da, Z. Peng, J. Tang, B. Kong, W.-B. Cai, Z. Yang, G. Zheng, *Adv. Energy Mater.* **2014**, *4*, 1400696.
[35] M. Gao, W. Sheng, Z. Zhuang, Q. Fang, S. Gu, J. Jiang, Y. Yan, *J. Am. Chem. Soc.* **2014**, *136*, 70774.
[36] L. Trotochaud, S. L. Young, J. K. Ranney, S. W. Boettcher, *J. Am. Chem. Soc.* **2014**, *136*, 67443.
[37] J. O. Bockris, T. Otagawa, *J. Phys. Chem.* **1983**, *87*, 29601.
[38] S. Trasatti, *Electrochim. Acta* **1984**, *29*, 15032.
[39] P. Strasser, S. Koh, T. Anniyev, J. Greeley, K. L. More, C. Yu, Z. Liu, S. Kaya, D. Nordlund, H. Ogasawara, M. F. Toney, A. Nilsson, *Nat. Chem.* **2010**, *2*, 454.
[40] S. Gupta, N. Patel, A. Miotello, D. C. Kothari, *J. Power Sources* **2015**, *279*, 620.
[41] N. Krstajić, M. Popović, B. Grgur, M. Vojnović, D. Šepa, *J. Electroanal. Chem.* **2001**, *512*, 16.
[42] K. Zeng, D. Zhang, *Prog. Energy Combust.* **2010**, *36*, 307.